ChemComm

High-Performance Supercapacitor Cells Based on ZIF-8 Derived Nanoporous Carbon Using Organic Electrolyte

Journal:	*ChemComm*
Manuscript ID	CC-COM-01-2016-000413.R1
Article Type:	Communication
Date Submitted by the Author:	19-Feb-2016

Complete List of Authors:	Salunkhe, Rahul; National Institute for Materials Science, World Premier International (WPI) Research Center for Materials Nanoarchitectonics (MANA) Young, Christine; National Institute for Materials Science, WPI Center for MANA Tang, Jing; National Institute for Materials Science, Takei, Toshiaki; National Institute for Materials Science (NIMS), International Center for Materials Nanoarchitectonics (MANA) Kobayashi, Naoya; National Institute for Materials Science, WPI Center for MANA Ide, Yusuke; NIMS, WPI-MANA Yamauchi, Yusuke; National Institute for Materials Science, WPI Center for MANA

Journal Name

COMMUNICATION

High-Performance Supercapacitor Cell Based on ZIF-8-Derived Nanoporous Carbon Using Organic Electrolyte

Received 00th January 20xx,
Accepted 00th January 20xx

DOI: 10.1039/x0xx00000x

www.rsc.org/

Rahul R. Salunkhe,[a] Christine Young,[a,b] Jing Tang,[a,b] Toshiaki Takei,[a] Yusuke Ide,[a] Naoya Kobayashi,[a] and Yusuke Yamauchi[a,b,*]

Low-cost supercapacitors have the ability to rapidly store a large amount of charge, which makes them the best alternative to batteries in portable electronics. Here, we demonstrate a fabrication of all-carbon supercapacitors using an organic electrolyte. By using ZIF-derived nanoporous carbon electrodes, we have realized a high-performance supercapacitor cell using a 2 M NEt_4BF_4/PC as an electrolyte. Our device shows good energy storage capacity comparable to other previously reported supercapacitors.

Many research efforts have been focused on different forms of carbon and its utilization as an electrode material for supercapacitor applications.[1] Various theoretical and experimental works have demonstrated deep understanding of the kinetics of ion diffusion through porous materials as well as importance for use of non-aqueous electrolytes.[2] Additionally, previous works have shown several critical effects of high surface area, pore-size distribution,[3] graphitic degree,[4] and nitrogen content[5] in order to obtain a high-performance electric double-layer capacitor (EDLC). However, the improvement of one property hampers other properties, thereby resulting in decreased or limited supercapacitor performance. Thus, most studies have focused on the development of optimized nanoporous carbon (NPC) materials that will lead to the greatly improved electrochemical performance of current EDLC materials.

Although there are many well-established methods for the synthesis of NPC materials, the NPCs obtained by direct carbonization of metal-organic frameworks (MOFs) have gained much attention for supercapacitor application.[6] MOF-derived carbons can retain the stable porous architecture required for electrochemical applications, and this method is simple and cost-effective. ZIF-8-derived NPCs can provide a high specific surface area (close to 2000 $m^2 \cdot g^{-1}$, **Table S1**), which is desired for supercapacitor application, with a unique architecture of polyhedron that may avoid the stacking/aggregation problem (due to multi-face) during electrode formation. Our previous studies of this material using aqueous electrolytes have demonstrated their potential for achieving a high-performance supercapacitor.[7] Based on these studies, we expect that the use of MOF-derived NPCs with an organic electrolyte having a minute ion size (<1 nm) can lead to achieving high specific energy and power, which are required in the device configuration for power electronics.

A recent theoretical study of NPCs demonstrated that the ratios of micropores and mesopores are important in achieving both high energy density and power density.[2c] Micropores are responsible for achieving high energy density and mesopores for achieving high power density. The MOF-derived NPCs possess both mesopores and micropores. Similar to that of, activated carbon (AC; ACS-679, China Steel Chemical Corp., Taiwan) utilized in industry (**Table S1**). Therefore, we are confident that we can fill concurrent demands for both high energy density and high power density in portable electronics. Accordingly, here we demonstrate the potential use of MOF-derived NPCs using non-aqueous electrolytes.

A large amount of ZIF-8 particles were synthesized by modifying previous methods. $Zn(CH_3COO)_2$ (0.176 g) and PVP (0.300 g) were dissolved in 20 ml of methanol to form a solution. 2-Methylimidazole (0.263 g) was dissolved in 20 ml of methanol to generate another clear solution. The above two solutions were cooled to 5°C for 1 h. Then the two solutions were mixed and aged at room temperature for 24 h. After 24 h, a white precipitate of ZIF-8 particles was observed, collected, washed with methanol, and dried.

Scanning electron microscope (SEM) images confirmed that the obtained ZIF-8 particles are composed of uniformly sized and dispersed crystals of rhombic dodecahedral shape (**Figure 1a,b**). The average size of ZIF-8 particles is around 1.5 µm. To cool the solutions before mixing is critical for the formation of uniformly sized ZIF-8 particles. Without cooling, uncontrolled random nucleation occurs, and the reaction rate is faster, resulting in non-uniform ZIF-8 particles (**Figure 1c**). The wide-angle XRD pattern is typical for a ZIF-8 crystal structure with unit cell parameters of $a=b=c=17.0605$ Å (**Figure 1d**).

a World Premier International (WPI) Research Center for Materials Nanoarchitectonics (MANA), National Institute for Materials Science (NIMS), 1-1 Namiki, Tsukuba, Ibaraki 305-0044, Japan
b Faculty of Science and Engineering, Waseda University, 3-4-1 Okubo, Shinjuku, Tokyo 169-8555, Japan
E-mail: Yamauchi.Yusuke@nims.go.jp
† Footnotes relating to the title and/or authors should appear here.
Electronic Supplementary Information (ESI) available:
See DOI: 10.1039/x0xx00000x

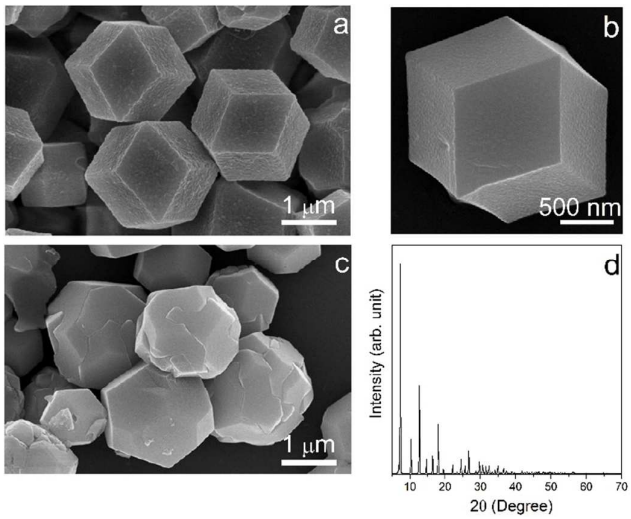

Figure 1. The (a) low- and (b) high-magnification SEM images of ZIF-8 particles obtained using our cooling approach. (c) Low-magnification SEM image of ZIF-8 particle without the cooling approach, showing irregularly shaped particles. (d) XRD pattern of ZIF-8 powder obtained using our cooling approach.

NPCs were prepared by the carbonization of ZIF-8 powder under the flow of nitrogen gas at 900°C. The ZIF-8 powders were homogeneously dispersed in a ceramic boat. The ceramic boat was then put into a tube furnace. The sample was exposed to a flow of nitrogen at room temperature for 1 h, and then the furnace was heated to the carbonization temperature at a heating rate of 5°C·min^{-1}. After reaching the targeted temperature, it was held for 5 h and then cooled to room temperature. The resultant black powders were collected and then washed three times with a 10 wt% of HF in aqueous solution to remove excess zinc. Finally, the carbon sample was rinsed with distilled water and then dried at 60°C overnight.

The SEM images for the NPCs are shown in **Figures S1a-b** and **S2a**. The original rhombic dodecahedral shape remains even after the thermal conversion to carbon. The wide-angle XRD pattern exhibited two broad diffraction peaks at 25° and 44°, which correspond to the (002) and (101) diffraction planes of graphites, respectively (**Figure S1c**).[7] The Raman spectra for NPC sample are shown in **Figure S1d**, exhibiting D and G bands centered at 1355 cm^{-1} and 1585 cm^{-1}, respectively, arising from the disordered carbon structures and graphitic carbon structure.[7]

The compositional analysis of this sample was carried out using TEM elemental mapping analysis (**Figure S2d–f**), showing that both carbon and nitrogen are well distributed over the surface. The porosity of our carbon was investigated by N_2 adsorption-desorption isotherms (**Figure S3**). The surface areas, pore volumes, pore-size distributions, and ratios of micropores and mesopores are summarized in **Table S1**. From the pore-size distribution (**Figure S3b**), it is revealed that the NPC possesses both mesopores (around 4 nm) and micropores (less than 2 nm). Both pores are confirmed by a high-resolution TEM image (**Figure S2b-c**). The NPC used in the present study has a very high surface area of 1873 m^2·g^{-1}, with the micropore surface area contribution as high as 46.8 %. For comparison, we investigated the porosity of commercially available AC, which has mostly been utilized in the supercapacitor industry. The AC is composed of smaller micropore surface area (43.4 %), to that of our NPC (**Table S1**). A high surface area is one of important criteria for achieving a high-performance EDLC supercapacitor. The surface area of our NPC is higher to that of AC as well as to those in recent reports about high-performance EDLC applications.[8] Thus, we expect to achieve high performance for a supercapacitor application using our NPC.

For preparation of the electrode, the NPC particle slurry was prepared and dropped onto the electrode surface. The electrode photograph is shown in **Figure 2a**. The thickness of this electrode was 20 μm, as observed from a cross-sectional SEM image of the electrode surface (**Figure 2b**). The film surface shows uniform and homogeneous dispersion without any cracks, due to its unique polyhedron shape.

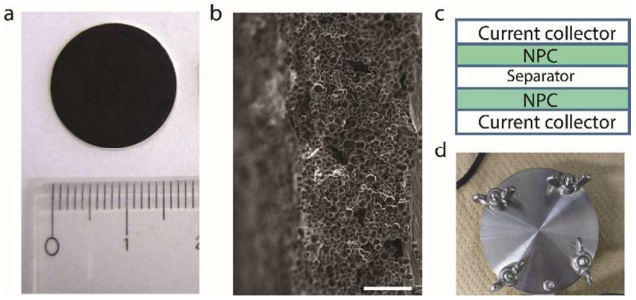

Figure 2. Actual device structure for electrochemical measurements. (a) Photograph of actual electrode used for cell. (b) Cross-sectional SEM image of NPC electrode (scale bar is 10 μm in length). (c) Device architecture with contact layers in planar structure. (d) Photograph for HS test cell.

The cyclic voltammetry (CV) studies were carried out in various voltage windows (up to 2.4 V) in order to understand capacitive behavior of this materials (**Figure S4a**). The mirror symmetric and stable CV shape is obtained for this supercapacitor cell within the potential window of 0.0 to 2.4 V. The typical CV curves for an NPC-based supercapacitor in a 2M NEt_4BF_4/PC electrolyte at different scan rates are shown in **Figure 3a-d**. The gravimetric and volumetric capacitance values can be calculated from the CV using the following equations:

$$C_g = \frac{1}{ms\,(V_f - V_i)} \int_{V_i}^{V_f} I(V)\,dV \qquad (1)$$

$$C_v = C_g \times \rho, \qquad (2)$$

where C_g is the gravimetric capacitance (F·g^{-1}), C_v is the volumetric capacitance (F·cm^{-3}), I is the current (A), v is the scan rate, V is the potential window, m is the mass (g), and ρ is the density (g·cm^{-3}).

At a scan rate of 10 mV·s^{-1}, the CV shape is quasi-rectangular, indicating a good capacitive behavior (**Figure 3a**). The volumetric and gravimetric capacitance values of the NPC-based supercapacitor cell were found to be 9.24 F·cm^{-3} and 21.0 F·g^{-1}, respectively. At a higher scan rate (500 mV·s^{-1}), the capacitance values were decreased at 2.25 F·cm^{-3}. The volumetric specific capacitances as a function of scan rate from 10 to 500 mV·s^{-1} are shown in **Figure 3e**. These values are comparable to the values reported in the literature for EDLC

cells[9] and biscrolled yarn supercapacitors (13 F·cm^{-3})[10] and are much higher than those of carbon-based microsupercapacitors (1.1 F·cm^{-3}).[11]

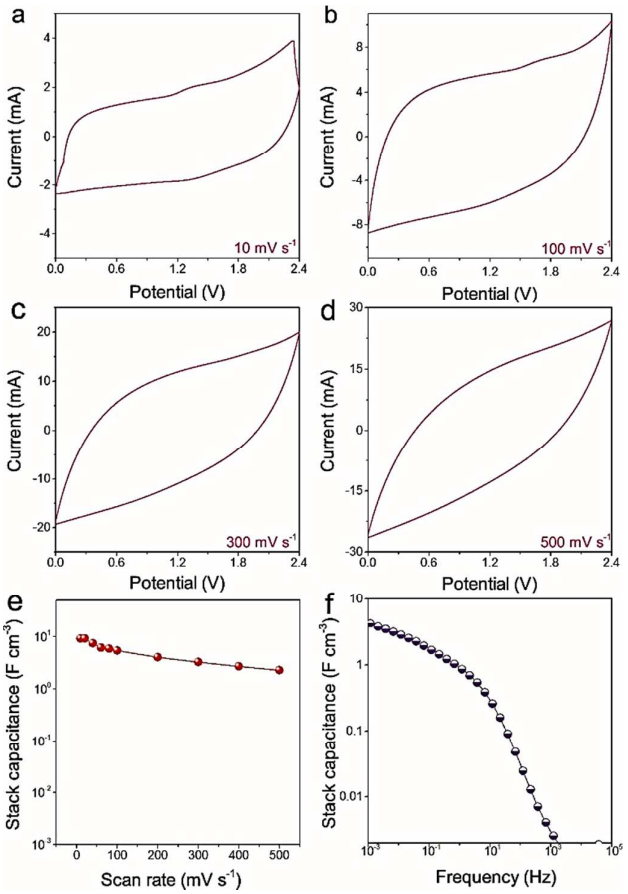

Figure 3. Electrochemical measurements for a supercapacitor cell. (a–d) CVs obtained for an NPC sample at various scan rates: (a) 10 mV·s^{-1}, (b) 100 mV·s^{-1}, (c) 300 mV·s^{-1}, and (d) 500 mV·s^{-1}. (e) Variation of stack capacitance with scan speed for NPC. (f) Capacitance *vs.* frequency plot obtained from EIS for tested EDLCs at a potential equal to the open circuit potential.

The unique shape of our NPC helps to maintain the discharge current by providing voids for ion intercalation and de-intercalation at a higher scan rate. This can be confirmed by the low equivalent series resistance (ESR) of this device (**Figure S5**). The ESR value is mostly due to an increased equivalent distribution resistance, which is caused by the diffusion of ions within the pores.[12] Additionally, the performance of our NPC was evaluated using high-frequency capacitive response in a frequency range of 1 mHz to 10^5 Hz (**Figure 3f**). The gravimetric[12] and volumetric capacitance values can be calculated from the imaginary part of the complex impedance spectrum using equations (2) and (3).

$$C_g = \frac{1}{2\pi f Z'' m} \qquad (3)$$

where C_g is the gravimetric capacitance (F·g^{-1}), m is the mass (g), f is the applied frequency, and Z'' is the imaginary part of impedance. For the NPC sample, the capacitance value is higher at low frequencies, and it starts to decrease after 0.01 Hz. This region corresponds to the transition between semicircles to straight-line in EIS spectra. The maximum capacitance value obtained at 0.001 Hz is 9.10 F·cm^{-3} (20.6 F·g^{-1}). Thus, the obtained capacitance values are almost identical to the values calculated from CV measurements.

The galvanostatic charge-discharge studies were carried out at various applied currents. A slight IR drop is observed at a relatively low applied current of 5 mA (**Figure S4b**). The charge-discharge curves show a slight IR drop after a potential of 2.2 V. Thus, the maximum potential limit for this electrode-electrolyte configuration is set to be 2.4 V. The gravimetric and volumetric capacitance values can be calculated from the galvanostatic charge-discharge using equations (2) and (4).

$$C_g = \frac{I \times \Delta t}{m \times \Delta V}, \qquad (4)$$

where C_g is the gravimetric capacitance (F·g^{-1}), I is the current (A), ΔV is the potential window, Δt is the discharge time, and m is the mass (g). The variation of stack capacitances with the applied currents is shown in **Figure S4c**. The maximum capacitance value obtained from the charge-discharge studies is 8.36 F·cm^{-3} (19.0 F·g^{-1}), which is consistent with the capacitance value obtained from CV and EIS analysis. On the other hand, an AC-based supercapacitor was also tested by CV and galvanostatic charge-discharge measurements (**Figure S4d-f**). The maximum capacitance was found to be 4.23 F·cm^{-3} (10.6 F·g^{-1}). Thus, the MOF-derived NPC is useful to attain more charge storage compared to that of AC. Unique three-dimensional polyhedron architecture with micro- and mesoporous structures helps to hold a more charge in porous voids. The high capacitance value as well as the low dependence of capacitances for an MOF-derived NPC with the applied currents is as seen in **Figure S4c** compared to that of the AC sample (**Figure S4f**).

A Ragone plot is an effective way to compare specific energy and specific power in different energy-storage devices. The specific energy (*SE*, Wh·g^{-1}), energy density (*ED*, W·h·cm^{-3}), specific power (*SP*, W·g^{-1}), and power density (*VE*, W·cm^{-3}) can be calculated using the following equations:

$$SE = \frac{\frac{1}{2}Cv^2}{3600} \qquad (5)$$

$$ED = SE \times \rho \qquad (6)$$

$$SP = \frac{3600 \times SE}{t} \qquad (7)$$

$$PD = SP \times \rho, \qquad (8)$$

where *C* is the gravimetric capacitance (F·g^{-1}), *v* is the scan rate, and ρ is the density (g·cm^{-3}). Our NPC-based supercapacitor cell shows a maximum volumetric energy of ~6.6 mWh·cm^{-3}, with a volumetric power of ~0.64 W·cm^{-3}.

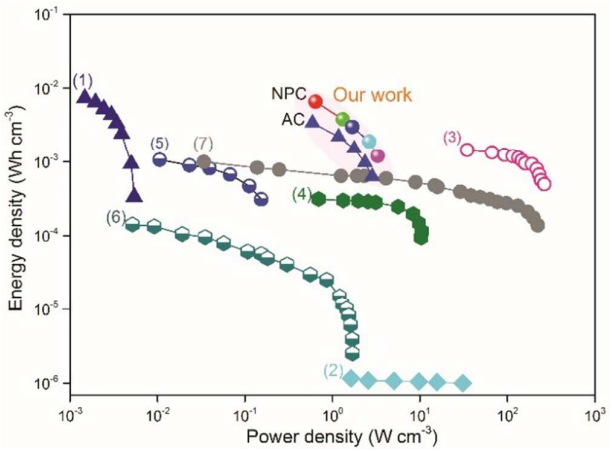

Figure 4. Comparative Ragone plot of the energy density and power density of our NPC-based supercapacitor cell with various previously reported materials: (1) Li thin-film battery,[11] (2) electrolytic capacitor,[11] (3) carbon onion microsupercapacitor,[11] (4) commercial supercapacitor,[11] (5) MXenes,[13] (6) reduced graphene-based MPG supercapacitor,[13] and (7) graphene-based microsupercapacitor.[13]

The comparison of our data with previously reported standard supercapacitor cells is shown in **Figure 4**. Compared to our device performance with carbon onions,[11] the MOF-derived NPCs have lower power density but higher energy density. Even though our device shows an energy density comparable to that of the lithium thin-film battery, two orders of magnitude higher power density is realized in our device. Compared to the AC-based supercapacitor, our device shows higher energy density, with comparable power density. More interestingly, the energy density value obtained for this device is much higher than those for other previously reported devices.

In summary, this work has demonstrated the importance of an MOF-derived NPC for achieving sufficiently high energy density and high power density for consumer electronic applications. The novel architecture with a high surface area and a designed micro- and mesoporous structure lead to high performance for the device application. In further research, we will focus on the development of NPCs with variable particle sizes and pore-size distributions, which are critical to achieving the desired performance. Various heteroatom doping in this carbon also promise to improve the conductivity.

Notes and references

1. (a) P. Simon, Y. Gogotsi, *Acc. Chem. Res.* 2013**, 46**, 1094; (b) M. Kaempgen, C. K. Chan, J. Ma, Y. Cui, G. Gruner, *Nano lett.* 2009**, 9**, 1872; (c) H. Jiang, P. S. Lee, C. Li, *Energy Environ. Sci.* 2013**, 6**, 41; (d) E. Frackowiak, F. Béguin, *Carbon* 2001, **39**, 937.
2. (a) J. Chmiola, G. Yushin, Y. Gogotsi, C. Portet, P. Simon, P. L. Taberna, *Science* 2006, **313**, 1760; (b) D. E. Jiang, Z. Jin, D. Henderson, J. Wu, *J. Phys. Chem. Lett.* 2012**, 3**, 1727 (c) J. Huang, B. G. Sumpter, V. Meunier, *Chem. Euro. J.* 2008, **14**, 6614.
3. (a) J. Chmiola, G. Yushin, R. Dash, Y. Gogotsi, *J. Power Sources* 2006, **158**, 765; (b) G. Gryglewicz, J. Machnikowski, E. Lorenc-Grabowska, G. Lota, E. Frackowiak, *Electrochimi. Acta* 2005, **50**, 1197.
4. N. L. Torad, R. R. Salunkhe, Y. Li, H. Hamoudi, M. Imura, Y. Sakka, C. C. Hu, Y. Yamauchi, Y. *Chem. Euro. J.* 2014, **20**, 7895.
5. (a) D. Hulicova, M. Kodama, H. Hatori, *Chem. Mater.* 2006, **18**, 2318; (b) R. R. Salunkhe, Y. H. Lee, K. H. Chang, J. M. Li, P. Simon, J. Tang, N. L. Torad, C. C. Hu, Y. Yamauchi, *Chem. Euro. J.* 2014, **20**, 13838.
6. (a) B. Liu, H. Shioyama, T. Akita, Q. Xu, *J. Am. Chem. Soc.* 2008, **130**, 5390; (b) J. Tang, R. R. Salunkhe, J. Liu, N. L. Torad, M. Imura, S. Furukawa, Y. Yamauchi, *J. Am. Chem. Soc.* 2015, **137**, 1572; (c) R. R. Salunkhe, J. Tang, Y. Kamachi, T. Nakato, J. H. Kim, Y. Yamauchi, *ACS Nano* 2015, **9**, 6288.
7. R. R. Salunkhe, Y. Kamachi, N. L. Torad, S. M. Hwang, Z. Sun, S. X. Dou, J. H. Kim, Y. Yamauchi, *J. Mater. Chem. A* 2014, **2**, 19848.
8. M. Lazzari, F. Soavi, M. Mastragostino, *J. Power Sources* 2008, **178**, 490.
9. (a) C. Masarapu, H. F. Zeng, K. H. Hung, B. Wei, *ACS Nano* 2009, **3**, 2199; (b) J. R. Miller, R. A. Outlaw, B. C. Holloway, *Science* 2010, **329**, 1637.
10. J. A. Lee, M. K. Shin, S. H. Kim, H. U. Cho, G. M. Spinks, G. G. Wallace, M. D. Lima, X. Lepro, M. E. Kozlov, R. H. Baughman, S. J. Kim, *Nature Commun.* 2013, **4**, 1970.
11. D. Pech, M. Brunet, H. Durou, P. Huang, V. Mochalin, Y. Gogotsi, P. L. Taberna, P. Simon, *Nature Nanotech.* 2010, **5**, 651.
12. P. L. Taberna, P. Simon, J. F. Fauvarque, *J. Electrochem. Soc.* 2003, **150**, A292.
13. M. Acerce, D. Voiry, M. Chhowalla, *Nature Nanotech.* 2015, **10**, 313.

Graphical abstract